JOURNAL OF SPACECRAFT AND ROCKETS
Vol. 47, No. 2, March–April 2010

Computational Flowfield Analysis over a Blunt-Body Reentry Vehicle

Antonio Viviani*
Seconda Università di Napoli, 81031 Aversa, Italy
and
Giuseppe Pezzella†
Centro Italiano Ricerche Aerospaziali, 81043 Capua, Italy

DOI: 10.2514/1.40876

This paper deals with aerodynamic and aerothermodynamic studies carried out to design a capsule vehicle suitable for the recovery of crew members from the International Space Station and/or from exploration missions to the moon or Mars. An integrated design tool called ENTRY is used to support vehicle reentry analysis and computational fluid dynamics design activities. A possible low-Earth-orbit reentry scenario, with the associated aeroheating environment, is generated and then analyzed. Several Euler and Navier–Stokes computations are performed to simulate the flowfield past the vehicle, for both perfect-gas and nonequilibrium reacting-gas models for the air. Numerical results and their comparison with flight data and wind-tunnel data are presented. An analysis of flowfields, obtained from numerical computations, is provided by means of flight forces and moments coefficients. Experimentally measured surface pressure distributions and aerodynamic coefficients compare rather well with numerical results.

Nomenclature

$\mathbf{A}^*$	=	axisymmetric terms matrix
A_f	=	forward Arrhenius constant, $m^3/kg\,mol\,s$
C_A	=	axial force coefficient
C_D	=	aerodynamic drag coefficient
C_L	=	aerodynamic lift coefficient
C_{My}	=	pitching moment coefficient
C_N	=	normal force coefficient
C_p	=	pressure coefficient
D	=	capsule diameter, m
D	=	aerodynamic drag, N
E_{af}	=	forward activation energy, J/kg mol
e	=	specific energy, J/kg
$\mathbf{F}$	=	flux vector
F	=	aerodynamic force, N
H	=	height, m
$\bar{h}$	=	mean value of the cell dimension, m
k_f	=	forward reaction-rate constant, $m^3/kg\,mol\,s$
L	=	length, m
L	=	aerodynamic lift, N
L	=	grid level
M	=	Mach number
M	=	aerodynamic moment, Nm
p	=	pressure, Pa
$\dot{q}$	=	heat transfer rate, W/m^2
Re	=	Reynolds number
R_b	=	capsule shoulder radius, m
R_N	=	heat-shield radius, m
S	=	surface, m^2
s	=	curve length, m
T	=	temperature, K
t	=	time, s
u	=	x velocity, m/s
V	=	velocity, m/s
V	=	volume, m^3
v	=	y velocity, m/s
$\mathbf{W}$	=	unknown state vector
w	=	z velocity, m/s
x	=	distance, m
x	=	Cartesian coordinate, m
y	=	Cartesian coordinate, m
z	=	Cartesian coordinate, m
α	=	angle of attack, deg
β	=	angle of sideslip, deg
β_f	=	forward temperature exponent
ε	=	emissivity, density ratio across the bow shock
γ	=	specific heat ratio
θ	=	flight-path angle, body-slope angle, deg
ρ	=	density, kg/m^3
φ	=	capsule sidewall angle, deg
$\mathbf{\Omega}$	=	source-term vector

Subscripts

a	=	atomic species
cg	=	center of gravity
cp	=	center of pressure
D	=	diameter
E	=	entry interface conditions
i	=	ith chemical species
inv	=	inviscid part
j	=	jth chemical species
o	=	zero lift, total reservoir condition
ph	=	peak heating conditions
ref	=	reference
S	=	surface
$t2$	=	stagnation-point conditions downstream of a normal shock wave
v	=	vibrational
vis	=	viscous part
w	=	wall conditions
∞	=	freestream conditions

Received 8 September 2008; revision received 3 December 2009; accepted for publication 6 December 2009.

*Professor, Fluid Dynamics, Dipartimento di Ingegneria Aerospaziale e Meccanica (DIAM), via Roma 29; antonio.viviani@unina2.it. Senior Member AIAA.

†Ph.D. Research Engineer, Aerothermodynamics and Space Propulsion Laboratory (ATER), via Maiorise; g.pezzella@cira.it. Member AIAA.

I. Introduction

THIS paper deals with the computational fluid dynamics (CFD) analyses of the flowfield past a Crew Return Vehicle (CRV) devised for the recovery of astronauts from the International Space Station (ISS) and/or from outer space exploration missions, such as those returning from the moon and Mars. Accurate numerical simulations, accounting for real-gas thermodynamics, transport properties variations, and finite rate chemical reactions (i.e., real-gas effects) are mandatory for a proper design of reentry vehicles, since the mentioned real-gas effects influence both vehicle aerodynamics and aerothermodynamics [1–3].

An Apollo-shaped capsule concept was considered as a possible CRV system, following the model proposed by NASA for the Crew Exploration Vehicle (CEV); this configuration seems to be the most natural option, because the Apollo vehicle is the only manned spacecraft that returned from the moon [4]. Moreover, in 1998, ESA successfully launched the Atmospheric Reentry Demonstrator (ARD), which was also an Apollo-like capsule. The ARD program was conducted primarily to validate existing and future ground-based experimental and numerical aerothermodynamic models [5].

In this way, the CRV development can take advantage of the huge amount of knowledge, both the experimental as well as the flight data, obtained from the Apollo program and then from the ARD program.

Moreover, the blunt-body design chosen for the CRV also follows from the fact that for reentries with an high value of specific energy (say, about 60 MJ/kg), a lower stagnation-point heating rate is the most important vehicle design parameter, rather than the high-cross-range and low-gravity-load capabilities experienced by a winged lifting configuration. Indeed, a design solution such as the space shuttle is still unrealistic, because it would demand a large mass for the heat shield, which has to withstand very high heating rates on the vehicle's leading edges, as well as to manage the high overall integrated heat load due to the long duration of lifting return trajectories compared with the ballistic ones. In fact, it is well known that the stagnation-point convective heat flux decreases with increasing nose radius [6]. In this framework, the detailed analyses of the flowfield around the CRV along the reentry trajectory, throughout extensive numerical simulations, play an important role within the space vehicle design [7,8].

Indeed, CFD simulations allow significantly reducing the number of in-flight and plasma wind-tunnel experimental test campaigns, as well as accounting for real-gas flow features, which are difficult to reproduce in ground-test facilities [6]. For example, CFD allows investigating the effects of the sonic line position shift, due to changes of the gas specific heat ratio γ, as well as the heat-shield surface catalycity on the vehicle aeroheating. The sonic line displacement is a very important aspect within the design process, since the vehicle's static aerodynamic instability markedly depends on the changing of the sonic line shape and location [9]. Moreover, at the vehicle surface, the thermal protection system could promote the recombination of the dissociated chemical species produced behind the strong bow shock [10]. These recombination reactions, through the releasing of the heat of formation of the molecular species leaving the heat-shield surface, increase the overall heat flux at the vehicle walls. Such augmented heat flux can be up to twice the value experienced by a noncatalytic wall [11,12]. The reliability of the numerical analyses, however, strongly requires that accurate wind-tunnel (WT) and flight data be used for code validation before the CFD code can be employed to predict flow phenomena.

The CRV reentry flight profile is evaluated by the ENTRY (entry trajectory) code, a design environment tool developed at the Dipartimento di Ingegneria Aerospaziale e Meccanica to support conceptual analysis and preliminary design phase of reentry missions. ENTRY evaluates, at the engineering level, the realistic flight conditions to be supplied as input for the vehicle flowfield calculations: for example, the freestream conditions of the reentry trajectory peak heating.

Several CFD simulations were performed with perfect-gas (PG) and reacting-gas (RG) models for the air to assess the CRV aerodynamics and aerothermodynamics in the framework of a low-Earth-orbit (LEO) reentry mission scenario. To this end, starting from the CRV reentry scenario assessment, axisymmetric and three-dimensional Euler and Navier–Stokes computations were performed with different wall boundary conditions [noncatalytic (NC), partially catalytic (PC), and fully catalytic (FC)] at the peak heating conditions of ballistic and lifting reentry trajectories, accounting for both cold-wall and radiative surface cooling.

Special attention is paid to numerical results and their comparison with flight data and WT data. The analysis of the flowfield obtained from numerical simulations has been also provided; in particular, the calculated aerodynamics coefficients are compared with the measured ones. Experimentally measured surface pressure distributions and aerodynamic coefficients compare rather well with results of the present computations.

II. Apollo-Like CRV Concept and the Reentry Flight Scenario

An Apollo-style capsule (see Fig. 1) of about 5 m in diameter, with a nose radius of 6.05 m, a sidewall angle of 33 deg, and an overall height of about 3.8 m has been investigated as a possible CRV. This vehicle concept represents a scaled-up version of the ARD capsule, which is a flying test bed successfully experimented by ESA in October 1998, on the top of the Ariane 503 launcher, to obtain accurate flight data for comparison with results from experimental and numerical tools used for space vehicle design through all phases of reentry flight [5]. The ARD was oversized to accommodate up to six crew members for the ISS. In particular, the capsule diameter was chosen to allow for the CRV/Ariane 5 integration, since the ESA launcher features a diameter of about 5.4 m.

The CRV reentry analysis from the ISS orbit was performed by using the ENTRY code. This code is capable of running descent trajectories with three degrees of freedom using the U.S. Standard Atmosphere (1976) and a nonrotating oblate Earth model when the vehicle aerodynamic database and its ballistic coefficient are available. To this aim, the ENTRY code quickly finds the Newtonian aerodynamic database of the reentry vehicle once its outer mold line (OML) is provided. ENTRY evaluates thermal environment, deceleration environment, cross range and down range performances, reentry corridor, and real-gas effects experienced by the space vehicle along the descent trajectory to obtain realistic flight conditions to supply as input to the numerical computations.

In the framework of a feasibility study, ENTRY suggests a ballistic coefficient of about 300 kg/m^2 for the CRV under consideration, because in order to maximize crew safety, a vehicle configuration with low ballistic coefficient is mandatory for high-energy reentries [4]. For this ballistic coefficient value, starting from the atmospheric entry interface, at $H_E = 120$ km with $V_E = 8$ km/s (inertial) and $\theta_E = -2$ deg, ENTRY provides the reentry flight scenario in the altitude-velocity plane, as reported in Fig. 2. In this figure, the iso-Mach and iso-Reynolds curves are shown, as they characterize aerodynamics and aerothermodynamics of the CRV. The continuous curve is a ballistic reentry trajectory and represents the worst case from the convective heat flux point of view. Along the dashed curve, the capsule is trimmed at an angle of attack (AOA) of about 20 deg,

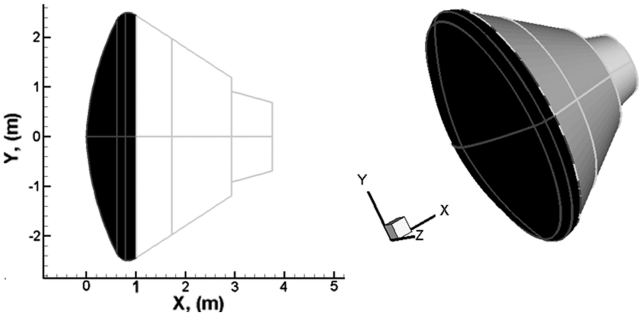

Fig. 1 Vehicle configuration with quotes and thermal-shield layout.

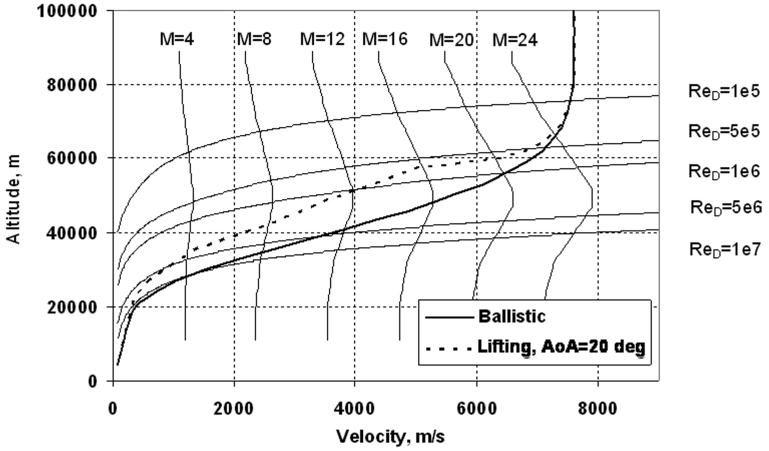

Fig. 2 Reentry flight scenario, starting from LEO orbit.

which is constant over the critical heating regime, thus employing aerodynamic lift to sustain the descent flight path (i.e., lifting return). These reentry trajectories are characterized by aerothermal environments that have to be accurately predicted for a reliable CRV aerodynamic heating assessment [13].

III. Flowfield Modeling and Numerical Solution

The physical mathematical model describing the flowfield around a hypervelocity vehicle includes balance equations for mass, momentum, total energy, and individual species. The full set of equations for a viscous compressible continuum flow in thermal and chemical nonequilibrium, assuming air to be a mixture of N_S perfect gases (i.e., the mixture species) and N_v vibrating species, can be written under the integral conservation form as follows [6]:

$$\frac{\partial}{\partial t}\int_V \mathbf{W}\,\mathrm{d}V + \int_S (\mathbf{F}_{\text{inv}} + \mathbf{F}_{\text{vis}})\cdot\mathbf{n}\,\mathrm{d}S + \frac{\Gamma}{r}\int_V (\mathbf{A}^*_{\text{inv}} + \mathbf{A}^*_{\text{vis}})\,\mathrm{d}V = \int_V \boldsymbol{\Omega}\,\mathrm{d}V \tag{1}$$

where

$$\mathbf{W} = [\rho, \rho u, \rho v, \rho w, e, \rho_1, \ldots, \rho_{Ns-1}, \rho e_{v1}, \ldots, \rho e_{vN_v}]^T$$

is the unknown state vector of the conserved quantities, where ρ is the fluid density; ρu, ρv, and ρw are the momentum densities; e is the total internal energy per unit mass; ρ_i and e_{vi} are, respectively, the density and the vibrational energy of the ith species; ρe_{vi} accounts for vibrational energy conservation; $\mathbf{F}$ is the flux vector, split into an inviscid and a viscous part, the expression of which is well known in literature [10] and therefore it is not written here, for simplicity; $\mathbf{A}^*$ is the axisymmetric terms matrix, split into an inviscid and a viscous part; Γ is equal to 1 for axisymmetric flows and 0 for 2-D and 3-D flows; and

$$\boldsymbol{\Omega} = [0, 0, 0, 0, 0, \Omega_1, \ldots, \Omega_{Ns-1}, \Omega_{v1}, \ldots, \Omega_{vN_v}]^T$$

is the source-term vector that defines mass and energy exchanges among species, as a result of the chemical reaction rate and of the energy transfer due to internal excitation. Hence, $\boldsymbol{\Omega}$ models the nonequilibrium processes. Finally, V is the arbitrary control volume cell, S is its closed boundary control surface, and $\mathbf{n}$ is the outward normal unit vector [10].

The computational analyses are performed by using the code H3NS, developed at the Aerothermodynamics and Space Propulsion Laboratory of the Centro Italiano Ricerche Aerospaziali [14]. The H3NS code solves the full Reynolds-averaged Navier–Stokes equations and considers the airflow in thermochemical nonequilibrium.

Several chemical kinetics models with five species (O, N, NO, O_2, and N_2) are implemented. Three dissociation reactions and two exchange reactions have been considered as reaction mechanisms, as reported in Tables 1 and 2, where M is the reacting partner (third body) [17]. Therefore, the reaction mechanism results in the system of 17 chemical reactions. The forward f reaction rates $k_{f,r}$ ($r = 1, \ldots, 17$) are expressed in the Arrhenius form, with the constants A_f, β_f, and E_{af} provided in Tables 1 and 2 for the kinetics models of Dunn–Kang (DK) and Park, respectively [15,16]. The energy exchange between vibrational and translational temperature

Table 1 Reaction-rate parameters with Dunn–Kang model [15]

No.	Reaction	$A_{f,r}$, m^3/kg mol s	$\beta_{f,r}$	$E_{af,r}$, J/kg mol	Third-body efficiency
1	$O_2 + M = 2O + M$	3.60×10^{15}	−1.0	4.938×10^8	$O_2 = 9$, $N_2 = 2$, O = 25, N = NO = 1
2	$N_2 + M = 2N + M$	1.92×10^{14}	−0.5	9.404×10^8	$O_2 = 1$, $N_2 = 2.5$, O = NO = 1, N = 0
3	$N_2 + N = 3N$	4.15×10^{19}	−1.5	9.404×10^8	——
4	$NO + M = N + O + M$	3.97×10^{17}	−1.5	6.286×10^8	$O_2 = N_2 = 1$, O = N = NO = 20
5	$NO + O = O_2 + N$	3.18×10^6	1.0	1.638×10^8	——
6	$N_2 + O = NO + N$	6.75×10^{10}	0.0	3.118×10^8	——

Table 2 Reaction-rate parameters with Park model [16]

No.	Reaction	$A_{f,r}$, m^3/kg mol s	$\beta_{f,r}$	$E_{af,r}$, J/kg mol	Third-body efficiency
1	$O_2 + M = 2O + M$	1.00×10^{19}	−1.5	4.947×10^8	$O_2 = N_2 = NO = 0.2$, O = N = 1
2	$N_2 + M = 2N + M$	3.00×10^{19}	−1.6	9.412×10^8	$O_2 = N_2 = NO = 0.233$, O = N = 1
3	$NO + M = N + O + M$	1.10×10^{14}	0.0	6.277×10^8	$O_2 = N_2 = 0.05$, O = N = NO = 1
4	$NO + O = O_2 + N$	2.40×10^6	1.0	1.598×10^8	——
5	$N_2 + O = NO + N$	1.80×10^{11}	0.0	3.193×10^8	——

is based on the Landau–Teller nonequilibrium equation, with average relaxation times taken from the Millikan–White theory as modified by Park (as discussed in [6]).

The viscosity coefficients for the single species, as well as the diffusion coefficients, are computed by means of Yun–Mason tabulated collision integrals, and the conductivity coefficients are computed by using Eucken's law; for the gas mixture, the coefficients are calculated using the semi-empirical Wilke formulas [6].

From the numerical point of view, the governing equations, together with the proper boundary conditions, are discretized using a cell-centered finite volume formulation on a structured multiblock grid. For the single-mesh cell, the discretized equation reads

$$\frac{\mathrm{d}\mathbf{W}_c}{\mathrm{d}t} + \frac{1}{V_c}\sum_{f=1}^{6}(\mathbf{F}_{c\mathrm{inv}} + \mathbf{F}_{c\mathrm{vis}})_f \cdot \mathbf{n} + \frac{\Gamma}{r}(\mathbf{A}^*_{c\mathrm{inv}}\mathbf{A}^*_{c\mathrm{vis}}) = \mathbf{H}_c \qquad (2)$$

where f is the index of the cell face, and c refers to the single cell of the computational domain.

The inviscid fluxes at cell interfaces are calculated by using a flux-difference-splitting Riemann solver, particularly suitable for high-speed flows.

The viscous fluxes are calculated by central differencing, i.e., computing the gradients of flow variables at cell interfaces by means of Gauss theorem. However, second-order accuracy is not automatically reached; for this reason, a second-order essentially non-oscillatory technique for the reconstruction of cell interface values is employed. The method is second-order-accurate in space. Time integration is performed by employing both an explicit single-stage (Euler forward) algorithm and an explicit five-stage Runge–Kutta scheme, coupled with an implicit evaluation of the chemical and vibrational source terms, under the hypothesis of time-marching approach to reach the steady solution for the flow. Sequential and parallel versions of the code are available.

Numerical analyses have been performed for all conditions of NC, PC, and FC surfaces for both cold-wall and radiative surface cooling. In the latter case, the wall temperature is calculated by Stefan–Boltzmann law and is updated explicitly at each streamwise station by means of a Newton–Raphson approach, usually achieving convergence within a few iterations.

IV. CRV Computational Flowfield Analyses and Comparison with WT and Flight Data

Axisymmetric and three-dimensional computations for both perfect and chemically reacting-gas approximation have been performed for the freestream conditions of Table 3. The far field is assumed to be made up of 79% of molecular nitrogen (N_2) and 21% of molecular oxygen (O_2).

In the following sections, several comparisons between present numerical results and numerical and experimental data (both from WT and flight) available in literature are provided. Moreover, for a more accurate assessment of the reliability of present results, several comparisons have been made with results from simplified solution methods, ranging from simple closed-form solutions to modified Newtonian (MN) methods.

A. Computational Grid

Computations have been carried out on multiblock structured grids generated with the tool ICEM-CFD. Each grid is tailored to account for the specific flow conditions of each case reported in Table 3. For example, Fig. 3 shows one of the grids designed to capture the flowfield around the CRV. Each mesh contains 32 blocks, for an overall number of about 750,000 cells (half-body only, since no sideslip velocity has been accounted for).

In particular, the mesh was initially generated algebraically and then adapted as the solution evolved, aligning the grid with the bow shock and clustering points in the boundary layer. This reduces the spurious oscillations in the stagnation area that are often observed in hypersonic flows, especially for large blunt-body flowfield computations. The distribution of surface grid points was dictated by the level of resolution desired in various areas of the vehicle, such as the stagnation region and base fillet, according to the computational aims. The value of the grid spacing near the wall was found to be on the order of 10^{-6} m to accurately predict heat transfer at the vehicle surface. Further, the number of grid points in the shoulder region was large enough to capture the rapid expansion that the flow experienced locally and to then accurately predict flow separation and the angle of the resulting shear layer. There are also sufficient points in the separated-flow region to resolve the vortical structure at the beginning of the wake flow.

B. Computational Results

To assess the reliability of present numerical analyses, a numerical rebuilding of ONERA S4 WT test, reported in [18], has been performed. The S4 tests campaign provided pressure profiles on the forebody centerline of the ARD capsule for assessment of the aerodynamics. The test reservoir conditions considered are $P_0 = 25$ bar and $T_0 = 1108$ K. These values are obtained at freestream conditions of $M_\infty = 10$, $P_\infty = 77.17$ Pa, $T_\infty = 55.70$ K, and $\alpha = 20$ deg, as summarized in Table 3. The aerodynamic pitching moment versus AOA is also provided.

Table 3 Freestream conditions of numerical computations

Run no.	Altitude, km	Mach	Pressure, Pa	Temperature, K	AOA, deg
1	50	10	79.78	270.65	0
2	57	19	32.78	255.27	0
3	67	22	8.18	227.08	0
4	57	19	32.78	255.27	10
5	57	19	32.78	255.27	17.5
6	57	19	32.78	255.27	20
7	62	22	16.68	241.53	20
8	57	19	32.78	255.27	28
9	57	16	32.78	255.27	28
10	57	12	32.78	255.27	28
			ARD trajectory points		
11	46	10	131.30	266.93	20
12	54	15	48.34	263.52	20
13	65	24	10.93	233.29	20
			ONERA S4 wind tunnel		
14	——	10	71.17	55.70	20
			AEDC tunnel C[a]		
15	——	10.18	——	——	——
16	——	10	——	——	——

[a]For run 15 $Re_D = 1.1 \times 10^6$, and for run 16, $Re_D = 1.2 \times 10^6$.

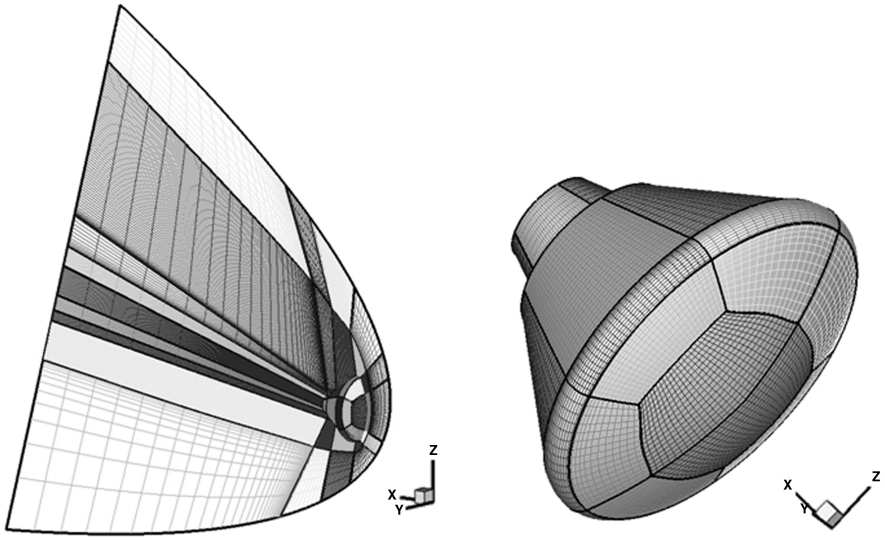

Fig. 3 Multiblock computational grid.

Recalling that experimental tests were performed with a flow total temperature of about 1100 K, the CFD simulations are performed with the perfect-gas model only. Results of present computations are summarized and compared with experimental data in Figs. 4–6.

The flowfield past the CRV is shown in Fig. 4, in which the Mach number contour field is plotted and compared with a schlieren image captured in the S4 facility. As shown, good agreement is obtained for bow shock standoff and curvature; this is an important prerequisite for the validation of a CFD code against experimental data.

As far as the pressure-field analysis is concerned, several comparisons for the pressure coefficient C_p are provided between present numerical results and numerical and flight data available for the Apollo and ARD capsules [5,18,19].

Indeed, the C_p allows absolute level comparisons between numerical reconstruction results and experimental data. Pressure coefficient comparisons between the present computation and the numerical and experimental data provided by Walpot [18] are given in Fig. 6, in which the comparison for the aerodynamic pitching moment coefficient is also shown. As shown in Figs. 4–6, experimental and numerical data compare rather well.

Next, comparisons between experimental and numerical results for four AOA (0, 10, 20, 28 deg) are reported in Fig. 7, which displays the pressure ratio P_w/P_{t2} on the capsule pitch-plane forward thermal shield for present results and WT experimental data provided in [19].

Experimental data available only for $\alpha = 0$ and 20 deg refer to a test performed in tunnel C at Arnold Engineering and Development Center (AEDC) at freestream Mach number 10.18 and Reynolds number $Re_{\infty D} = 1.1 \times 10^6$ [19]. As a further comparison, the pressure distribution P_w on the capsule centerline can be evaluated with the MN theory that gives

$$\frac{P_w}{P_{t2}} = \sin^2\theta + \frac{P_\infty}{P_{t2}}\cos^2\theta \tag{3}$$

As one can see, numerical, experimental, and theoretical data agree well for all AOA.

It is worth noting that differences between the numerical and MN pressures at the capsule corner (i.e., at $s/R_b = 0.965$) are due to the vehicle's forebody, which is a truncated spherical cap. This means that the streamwise velocity gradients must be relatively large (above

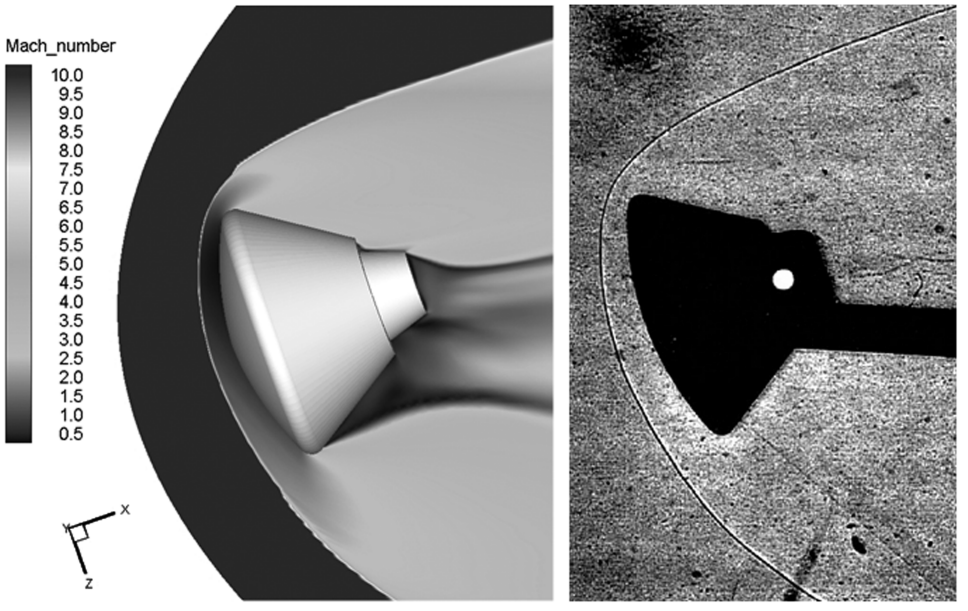

Fig. 4 Mach number computed contours and comparison with the ARD schlieren photograph taken in the ONERA S4 WT for $M_\infty = 10$ and $\alpha = 20$ deg ($P_0 = 25$ bar) [18].

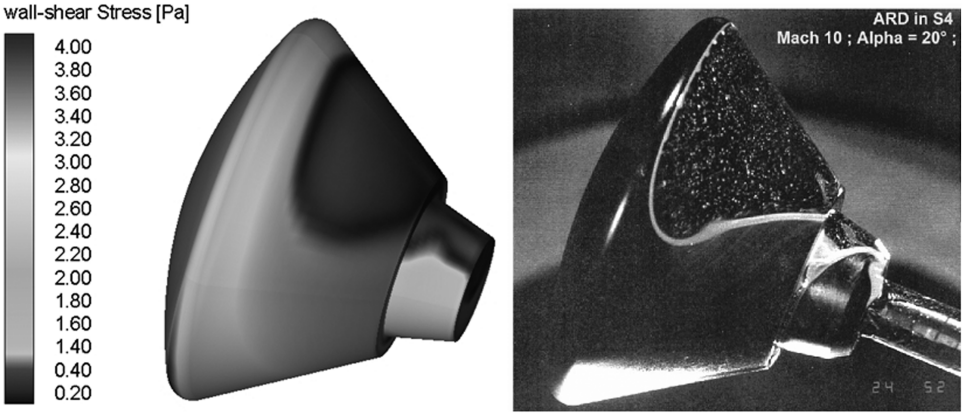

Fig. 5 Wall shear stress; comparison with ARD oil flow patterns in the ONERA S4 WT [18].

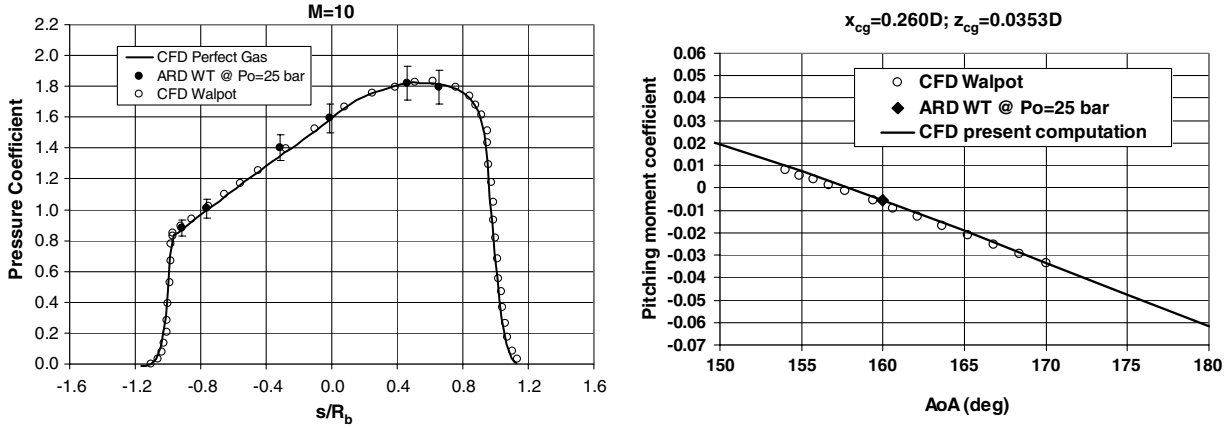

Fig. 6 Pressure coefficient at forebody centerline (left) and pitching moment coefficient (right); comparison among present computations and data provided by Walpot [18].

the value needed for a full hemisphere) to produce sonic flow at the capsule corner [19] and, as is well known, that the heat flux increases at the capsule corner, as shown in Fig. 8. This figure shows the comparison of the heat flux at the capsule forebody centerline between present results and heating rates measured in tunnel C for a nominal freestream Mach number of 10 and for freestream Reynolds number, based on the model's body diameter, of 1.2×10^6 [19].

Figure 9 shows present CFD results and flight-data comparisons at the ARD trajectory point at Mach 10 and $\alpha = 20$ deg [5]. As shown, the numerical reconstruction refers to PG and nonequilibrium computations, whereas the error bars associated with flight data accounts for uncertainties of preflight aerodynamic database (drag coefficients), measurements, and atmospheric-pressure dispersion [5].

Real-gas effects are clearly displayed in the stagnation region. Figure 10 displays CFD results and ARD flight-data comparison at the ARD trajectory point at Mach number 15 [5]; the magnitude of real-gas effects is increased at this flight condition, compared with the case of Mach 10. Real-gas effects, however, are maximized at a Mach number of 24, as displayed in Fig. 11. Therefore, Figs. 9–11 suggest that CFD results compare rather well with flight data for both PG and RG computations.

In particular, as shown in Fig. 12, in which C_p profiles at various Mach numbers are provided, numerical computations are able to describe the differences between RG and PG, which increase with the altitude along the ARD reentry trajectory. Indeed, the main impact on the pressure coefficient is localized in the stagnation-point region and in the windward and leeward expansion zones. The stagnation point shifts in the direction of the windward side and the stagnation pressure increases with the Mach number. The C_p level of the leeward shoulder (tore) decreases with the Mach number, whereas on the windward tore, it is stronger when the Mach increases.

C. Preliminary Assessment of CRV Aerodynamics

The analysis of the CRV aerodynamics is given in terms of lift C_L, drag C_D, and pitching moment C_{My} coefficients, as they are of primary interest for an axisymmetric capsule. They are defined by

$$C_i = \frac{F_i}{\frac{1}{2}\rho_\infty V_\infty^2 S_{\text{ref}}} \qquad i = L, D \tag{4}$$

$$C_{Mj} = \frac{M_j}{\frac{1}{2}\rho_\infty V_\infty^2 L_{\text{ref}} S_{\text{ref}}} \qquad j = Y \tag{5}$$

The reference parameters chosen for the definition of aerodynamic forces and moment coefficients are the longitudinal reference length ($L_{\text{ref}} = D = 2R_b$) equal to the capsule diameter (e.g., 5.0 m), and the reference area ($S_{\text{ref}} = \pi R_b^2 = 19.6$ m^2), equal to the maximum cross-sectional area of the CRV. The pitching moment is computed from the vehicle nose. The CRV aerodynamic database (AEDB) has been generated for the following ranges (see Fig. 2): $3 \le M_\infty \le 24$, $150 \le \alpha \le 180$ deg, $10^5 \le Re_{\infty D} \le 10^7$, and $\beta = 0$ deg (no lateral directional analysis has been considered).

The curves of lift, drag, aerodynamic efficiency, and pitching moment coefficients for α ranging from 150 to 180 deg are shown in Figs. 13–16. Note that α is measured from the capsule apex as done in the past for the Apollo command module aerodynamics development [20].

Figures 13–16 show comparisons of present CFD results summarized in Table 4, experimental data provided in [20], and results of the MN theory, obtained for different specific heat ratios γ. Because of the simple geometric shape of CRV, the MN theory is easily used to give the drag coefficient of the CRV at zero lift:

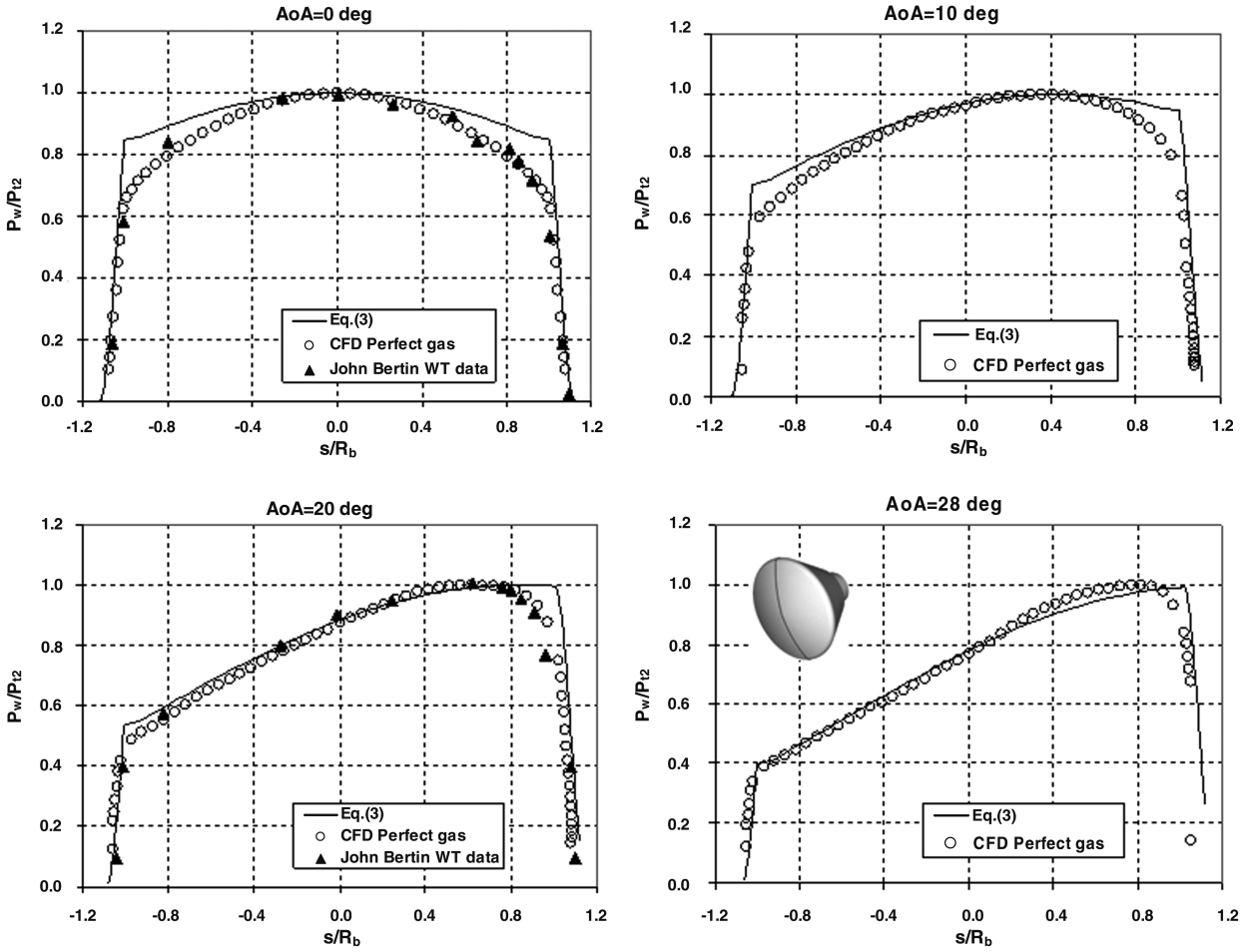

Fig. 7 Pressure distribution in the capsule pitch plane for four AOA (i.e., 0, 10, 20, 28 deg); comparison among MN, present CFD results, and WT data [19].

$$C_{Do} = \frac{2\pi}{S_{\text{ref}}} \int_0^{\eta} C_p r^2 \sin\eta \cos\eta \, d\eta = \frac{(2-\varepsilon)}{2}(1+\cos^2\eta) \qquad (6)$$

where $\eta = \sin^{-1}(R_b/R_N)$, and $\varepsilon = \rho_1/\rho_2$ is the density ratio across the bow shock at the stagnation point.

Lift, drag, and pitching moment coefficients read

$$C_D = C_{Do} + 12(1-C_{Do})\sin^2\frac{\alpha}{2} - 6(6-5C_{Do})\sin^4\frac{\alpha}{2} + 4(6-5C_{Do})\sin^6\frac{\alpha}{2} \qquad (7)$$

$$C_L = [2(1-C_{Do}) - (3-\tfrac{5}{2}C_{Do})\sin^2\alpha]\sin\alpha \qquad (8)$$

$$C_{My_{\text{nose}}} = -\frac{x_{\text{cp}}}{L_{\text{ref}}} C_Y = -\frac{(2-\varepsilon)}{2L_{\text{ref}}} x_{\text{cp}} \cos\alpha \sin\alpha \sin^2\eta \qquad (9)$$

where x_{cp} is the abscissa of the center of pressure that is influenced, as is well known, by the real-gas effects [2].

The different results compare rather well. Moreover, since the pitching moment derivative $C_{M\alpha}$ is negative, the CRV is statically stable for α ranging from 150 to 180 deg, provided that the capsule's center of gravity is close to the moment reference point. To further verify the reliability of CRV aerodynamics, Figs. 17 and 18 compare

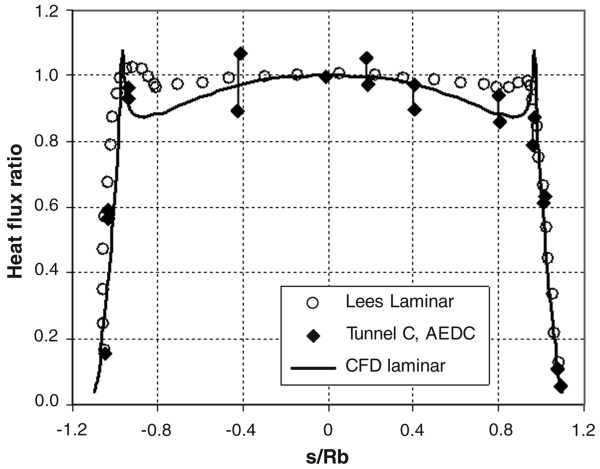

Fig. 8 Heat flux distribution on the forebody centerline; comparison among present, WT [19], and Lees [22] data.

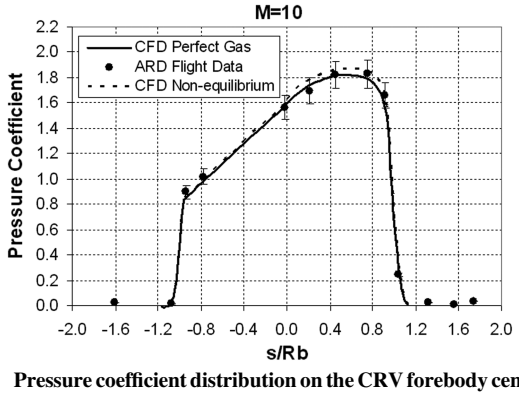

Fig. 9 Pressure coefficient distribution on the CRV forebody centerline at $M_\infty = 10$; comparison among present CFD results and ARD flight data [5].

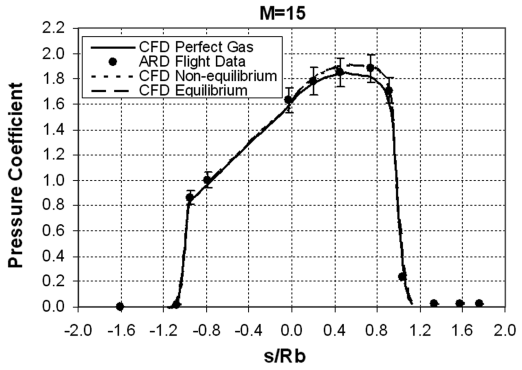

Fig. 10 Pressure coefficient distribution on the CRV forebody centerline at $M_\infty = 15$; comparison among CFD and ARD flight data [5].

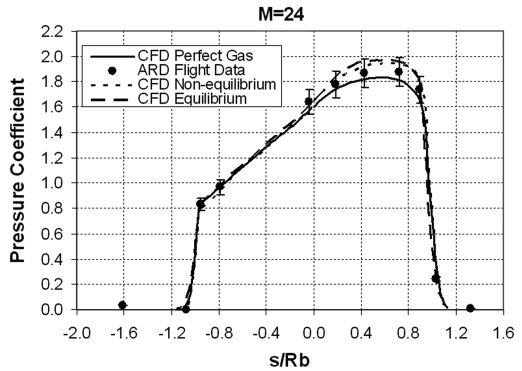

Fig. 11 Pressure coefficient distribution on the CRV forebody centerline at $M_\infty = 24$; comparison among CFD and ARD flight data [5].

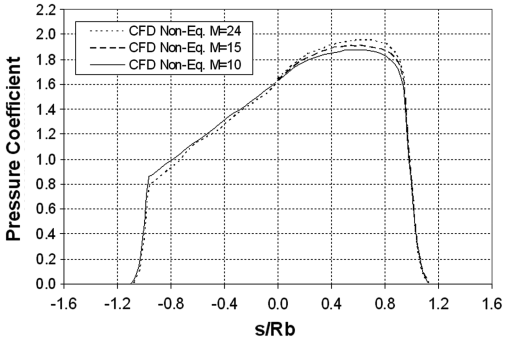

Fig. 12 Pressure coefficient distribution on the CRV forebody centerline at $M_\infty = 10$, 15 and 24.

the present numerical results with the ARD aerodynamics flight-data (AEDB) reconstruction [5].

As shown, the trends of both axial force C_A and normal force C_N coefficients are consistent with the experimental data. In particular, with reference to the axial force coefficient, the CFD PG values do not match the reconstructed values, which are closer to the CFD RG values, thus suggesting a relevance of real-gas effect in flight.

On the other hand, for the normal force coefficient, the discrepancy between present CFD results and flight data seems low. Moreover, the CFD results/flight-data matching for C_N seems to be the best when a nonequilibrium assumption is considered, whereas for C_A, matching the best is for the equilibrium assumption. This can be explained by recalling that C_N is more sensitive than C_A to the pressure flowfield on the rear conical part of the capsule; that part of the vehicle is quite difficult to compute, and the comparison with flight results in terms of pressure field is not as good, and so the present CFD results for C_N cannot be considered as fully realistic [5].

As far as flow chemistry effects are concerned, it is worth noting that CFD results reported in Table 4 involve both Dunn–Kang and

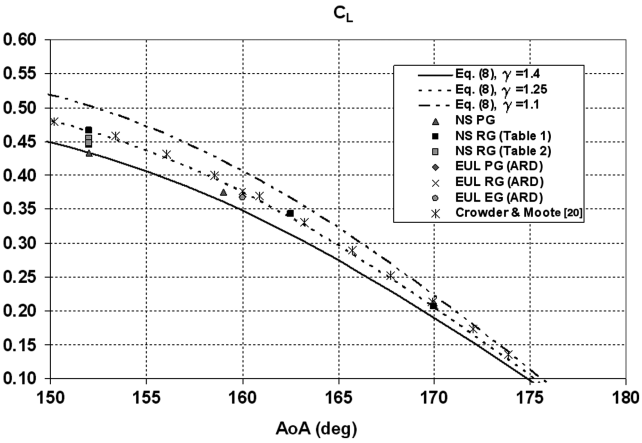

Fig. 13 Lift coefficient; comparison between present CFD, theoretical, and experimental results.

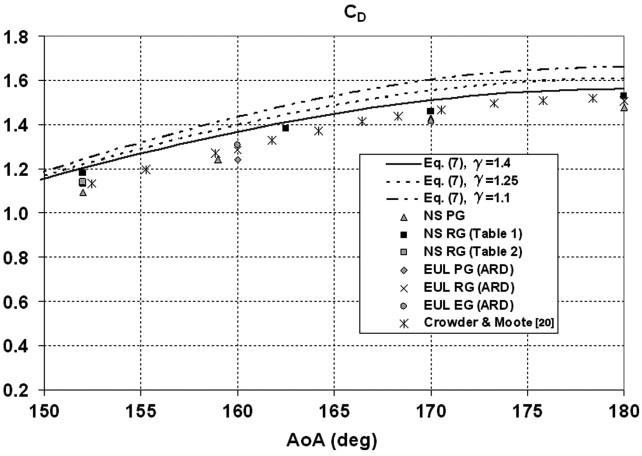

Fig. 14 Drag coefficient; comparison between present CFD, theoretical, and experimental results.

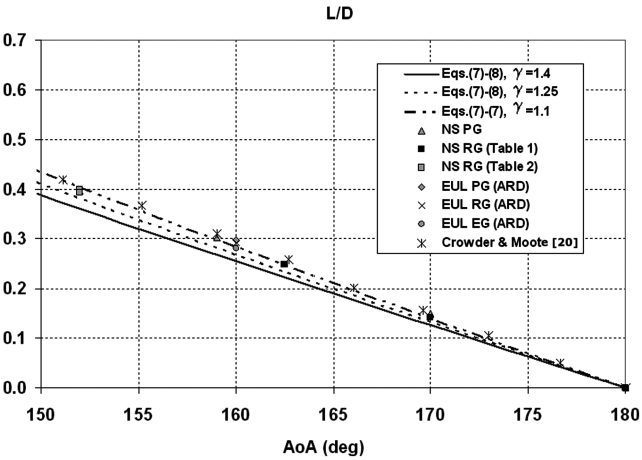

Fig. 15 Aerodynamic efficiency; comparison between CFD, theoretical, and experimental results.

Park chemical kinetics models. Thus, the effects of finite rate chemistry on the CRV aerodynamics can be appreciated. Results summarized in Table 4 (see also Figs. 13–16) show that there are no significant differences when switching from Dunn–Kang to Park kinetics.

In particular, the effects of both chemical reactions and their kinetics on CRV aerodynamics at $M_\infty = 16$ and 19 for $\alpha = 28$ deg can be recognized in Figs. 19 and 20. Figure 19 confirms that for both

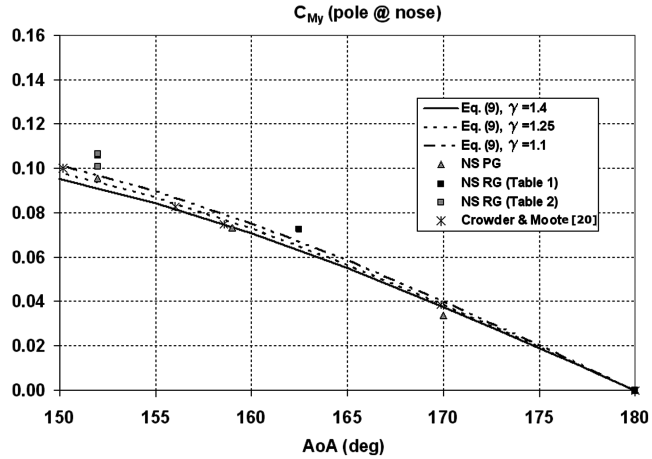

Fig. 16 Pitching moment coefficient; comparison between CFD, theoretical, and experimental results.

Mach numbers, MN theory results compare well with reacting-gas results, provided that they are within MN and PG estimations. Instead, for the effect of chemical kinetics, the left side of Fig. 20 highlights that at $M_\infty = 16$, no differences are expected for the aerodynamic coefficients switching from Dunn–Kang kinetics to Park kinetics. However, at $M_\infty = 19$, both lift and drag coefficients increase when we change the gas model from the PG model to the Dunn–Kang or Park kinetics. Considering only the latter kinetics model, a difference of about 2% is observed on the value of C_L and of about 5% on the value of C_{My}. These conclusions are confirmed by Fig. 20, in which the vehicle center-of-pressure abscissa x_{cp}, with respect to the MN estimation, is given. Figure 20 shows that at $M_\infty = 16$, the value of x_{cp} for the PG solution decreases by about 10% with respect to the MN estimation.

At this Mach number, however, there is no difference between values provided by the two chemical kinetics models. At $M_\infty = 19$, instead, even though the value of x_{cp} for the PG solution decreases again by about 10% with respect to the MN estimation, Dunn–Kang and Park models provide values differing from each other by about 2%. The latter difference is dangerous if neglected in the design of capsule thermal-shield layout.

Finally, the Mach number effect on the capsule aerodynamics can be recognized in Fig. 21. It can be observed that for a fixed value of α (i.e., 152 deg), assuming the Dunn–Kang kinetics, an increase in the Mach number causes a slight reduction of C_L and C_D, whereas their ratio and the values of C_{My} remain practically constant. For example, when the Mach number is increased from $M_\infty = 12$ to 19, C_L and C_D decrease by about 4.5%. On the contrary, with the Park's kinetics, if Mach increases from 16 to 19, C_L increases and C_{My} decreases, whereas C_D does not change.

Table 4 CRV aerodynamics: drag, lift, aerodynamic efficiency, and pitching moment coefficient as a function of the test case considered (Mach, flow model, and AOA)

Mach	Flow model	AOA, deg	C_D	C_L	L/D	C_{My}
10	PG	180	1.4760	0.0000	0.0000	0.0000
10	RG (Table 1)	180	1.5300	0.0000	0.0000	0.0000
12	RG (Table 1)	152	1.1814	0.4664	0.3948	0.1064
16	PG	152	1.0965	0.4339	0.3957	0.0964
16	RG (Table 1)	152	1.1392	0.4479	0.3932	0.1067
16	RG (Table 2)	152	1.1389	0.4480	0.3934	0.1066
19	PG	170	1.4300	0.2104	0.1471	0.0341
19	RG (Table 1)	170	1.5000	0.2143	0.1429	0.0424
19	PG	160	1.2420	0.3770	0.3024	0.0733
19	RG (Table 1)	162.5	1.3800	0.3437	0.2491	0.0728
19	PG	152	1.0940	0.4328	0.3956	0.0956
19	RG (Table 1)	152	1.1315	0.4456	0.3938	0.1060
19	RG (Table 2)	152	1.1386	0.4541	0.3988	0.1008

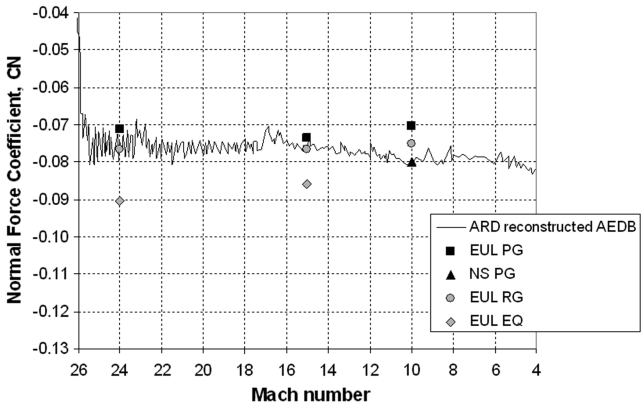

Fig. 17 Normal force coefficient; comparison among present CFD and ARD reconstructed aerodynamics data (AEDB) [5].

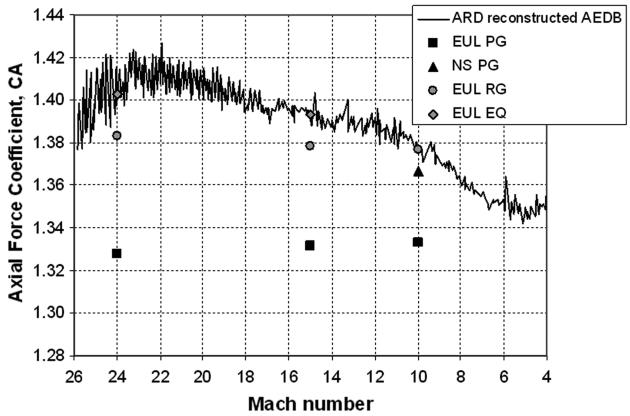

Fig. 18 Axial force coefficient; comparison among present CFD and ARD reconstructed aerodynamics data (AEDB) [5].

D. Preliminary Assessment of CRV Aerothermodynamics

The aerothermal loading environment corresponding to the flight scenario proposed for the CRV is summarized in Fig. 22, which shows plots of the stagnation-point heating rate versus the altitude in the case of both lifting and ballistic descent. The heat flux profiles at radiation equilibrium ($\varepsilon = 0.85$) were provided for NC, PC, and FC wall boundary conditions. When CRV performs the lifting reentry, the peak heating occurs at $H_{\text{ph}} = 62$ km and $M_{\text{ph}} = 22$ conditions and is equal to about 372 kW/m^2 when the heat-shield wall is supposed to be FC. If the wall is NC, a value of 245 kW/m^2 is foreseen, and for a PC wall, the heat flux is 275 kW/m^2.

However, the peak heating of the reference ballistic trajectory is attained at $H_{\text{ph}} = 57$ km and $M_{\text{ph}} = 19$ conditions and is equal to about 430 kW/m^2 in the case of a FC wall; it is about 280 kW/m^2 when the wall is NC, whereas in the case of a PC wall, the peak heat flux reaches about 325 kW/m^2.

Once freestream conditions of trajectories' peak heating were provided, a number of Navier–Stokes computations were performed in the case of nonequilibrium reacting gas by alternatively considering the heat-shield surface as NC, PC, and FC. Computations refer to the capsule surface both for cold-wall and for radiative equilibrium temperature conditions. No heat-shield ablation and recession were considered herein.

Figure 23 shows comparisons of the convective heat flux along the forebody centerline between the cases of FC and NC cold walls ($T_w = 300$ K) evaluated at the peak heating conditions of the ballistic trajectory for $\alpha = 0$ deg. Note that the bold continuous line is the capsule forebody centerline so that x and y coordinates help the reader to localize the heat flux profile on the vehicle OML (refer also to Fig. 1). As shown, the ratio $(\dot{q}_{FC}/\dot{q}_{NC})_w$ of heating for FC over that for NC is equal to about 1.5. It is expected to decrease when the wall

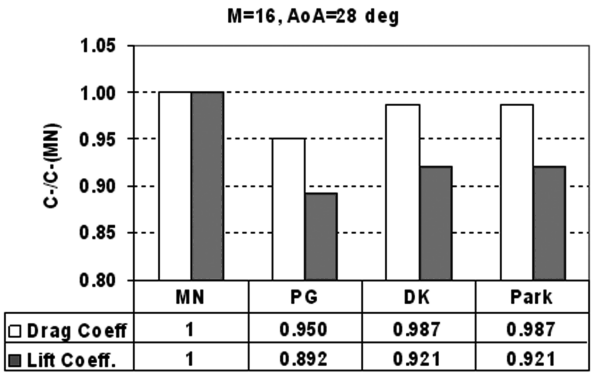

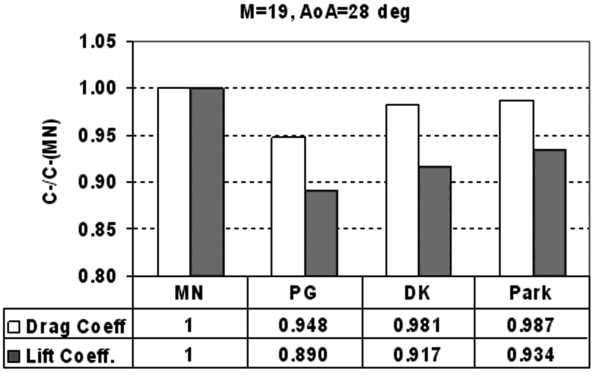

Fig. 19 Effect of chemical reactions and kinetics at $\alpha = 28$ deg for $M_\infty = 16$ and 19; comparison among MN, PG, DK, and Park computations.

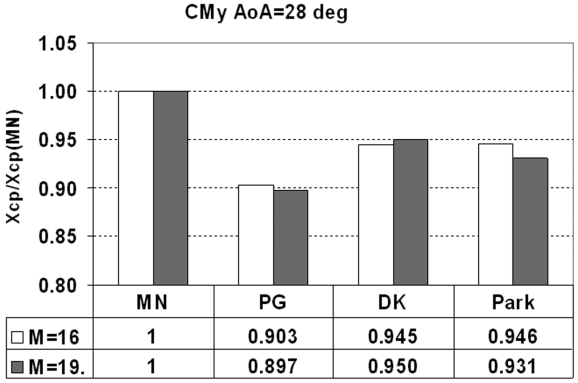

Fig. 20 Effect of chemical reactions and kinetics on x_{cp} at $\alpha = 28$ deg for $M_\infty = 16$ and 19; comparison among MN, PG, DK, and Park computations.

temperature increases, but in any case, it will be higher than the case of an adiabatic radiative equilibrium wall (see Fig. 24).

A catalytic effect can be appreciated as well, since in the case of an FC wall, atoms fully reassociate due to the cold-wall temperature hypothesis. To appreciate the effect of the chemical species diffusion toward the wall, Fig. 23 also reports both the conductive and the chemical contributions to the FC heat flux.

Figure 23 confirms that the capsule sidewall corner, as known, is the hottest vehicle part, especially when the CRV is flying trimmed at a nonzero AOA, as shown in Fig. 24, in which heat flux profiles on the capsule forebody are reported for $\alpha = 20$ deg.

Figure 24 shows the comparison of the heat flux along the forebody centerline at surface radiative cooling conditions ($\varepsilon = 0.85$) with the cases of FC, PC, and NC walls at the peak heating conditions of both ballistic and lifting reentry.

In conclusion, both Figs. 23 and 24 confirm that overheating caused by catalytic action is potentially very large compared with the case of an NC wall. Moreover, the largest difference occurs at the sphere-cone junction (corner fillet), where large changes occur in the flow gradients along the surface. Therefore, the corner radius represents the dominant geometric feature for the convective heating, instead of the usual heat-shield radius of curvature, R_N. Indeed, the peak heating does not occur at the stagnation point, which is on the spherical cap, but on the capsule's toroidal surface.

Finally, Fig. 25 shows the static pressure contours distribution on the capsule surface and surface streamlines, which highlight the complexity of the flow structure as, for example, the separation bubble that is generated at the vehicle afterbody (left side of Fig. 25). As one can see, the flow remains attached on the windward side of the

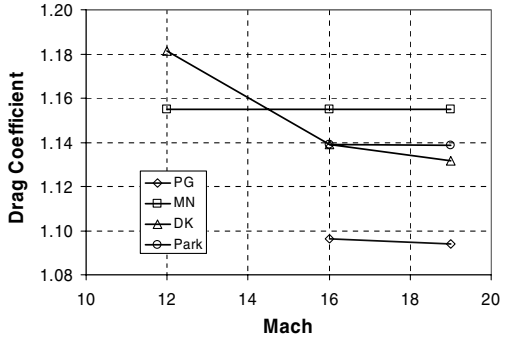

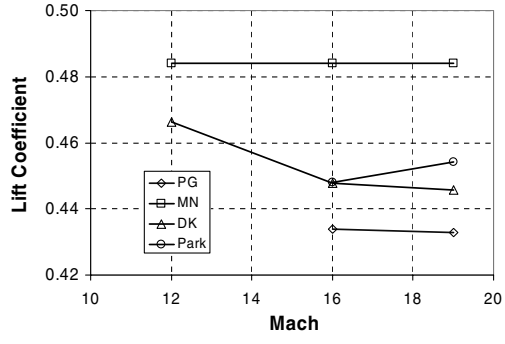

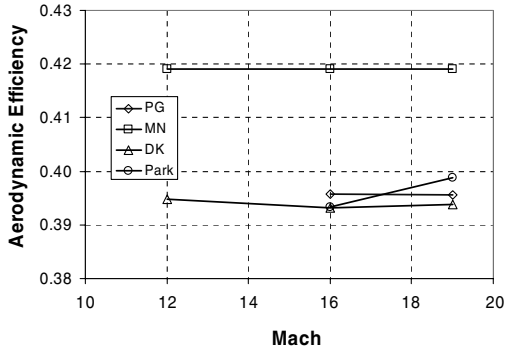

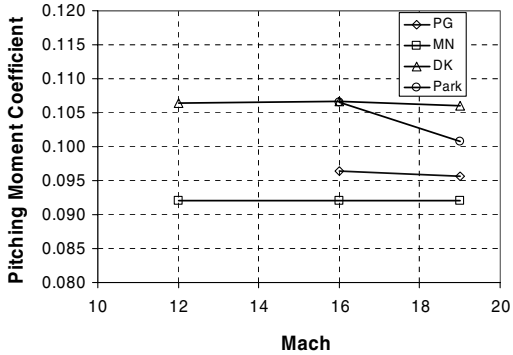

Fig. 21 Effect of chemical kinetics on capsule aerodynamics at $\alpha = 28$ deg vs Mach number; comparison among MN, PG, DK, and Park computations.

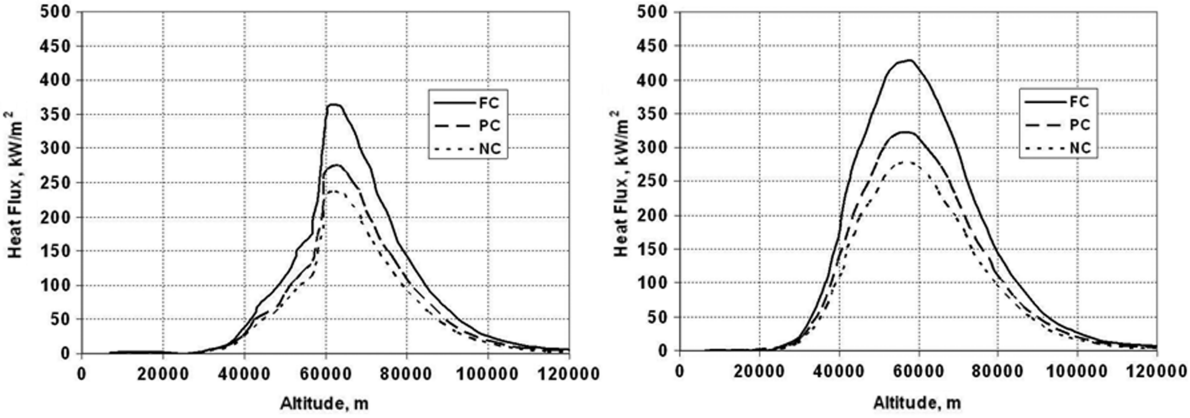

Fig. 22 Vehicle aeroheating environment for lifting (left) and ballistic (right) reentry.

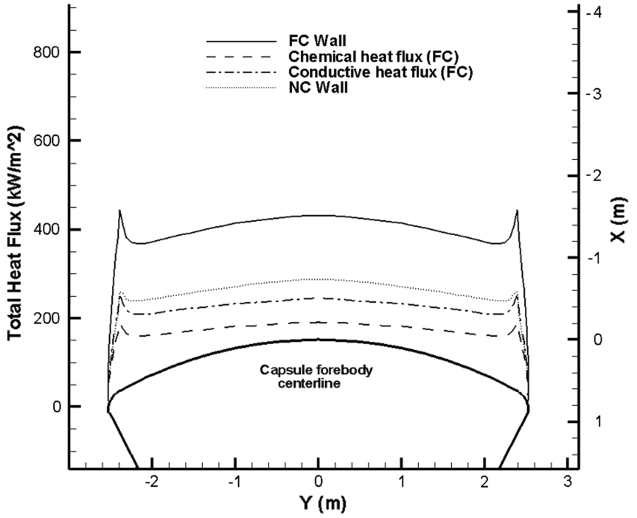

Fig. 23 Heat flux on the CRV forebody centerline for $\alpha = 0$ deg, $M_\infty = 19$, $H = 57$ km, and $T_w = 300$ K.

conical afterbody, whereas separation occurs near the maximum diameter point on the CRV shoulder. It should be noted that knowledge of this point is relevant for the capsule afterbody aeroheating assessment.

E. Reliability of CFD Results

All CFD results provided in this paper refer to both converged and grid-independent computations, as described hereinafter. To assess numerical solution convergence, both equation residuals and aerodynamic coefficients (i.e., C_L, C_D, and C_{My}) and the stagnation-point heat flux have been monitored during iterations. Solution convergence is assumed when equation residuals drop more than three orders of magnitude and both the aerodynamic coefficients and the stagnation-point heat flux plots are flat for enough time.

As an example, the convergence histories of drag coefficient and of stagnation-point heat flux in the case of $M_\infty = 19$, $H = 57$ km, and $\alpha = 0$ deg are reported in Fig. 26. As one can see, the numerical computation is stopped and assumed to converge at about 300,000 iterations, since the plotted curves look flat.

As far as grid convergence analysis is concerned, mesh sensitivity analyses have been carried out on three levels of the structured multiblock grid (L_1, L_2, and L_3) and the Richardson extrapolation criterion has been applied. The medium grid L_2 is obtained by halving the size of cells of the coarse L_1 grid, and so the number of cells of L_2 is eight times larger than the number of cells of L_1. Similarly, the finer grid L_3 is obtained by halving the size of cells of the medium grid, and so its number of cells is 64 times larger than the number of cells of L_1.

As a numerical strategy, the single computation is started on the coarsest grid level and then, when a satisfying level of accuracy has been reached, the solution is successively interpolated on finer grids and restarted. Hundreds of thousands of iterations have been necessary to reach solution convergence, both in terms of steady-state solution and grid independence of results.

If the solution is in the asymptotic range of convergence, it is possible, by means of the Richardson extrapolation criteria, to estimate the value of a global (C_L, C_D, etc.) or a local (pressure, etc.) solution functional f at virtually zero cell dimension ($\bar{h} = 0$), i.e., at an infinite number of cells. This value can be obtained by

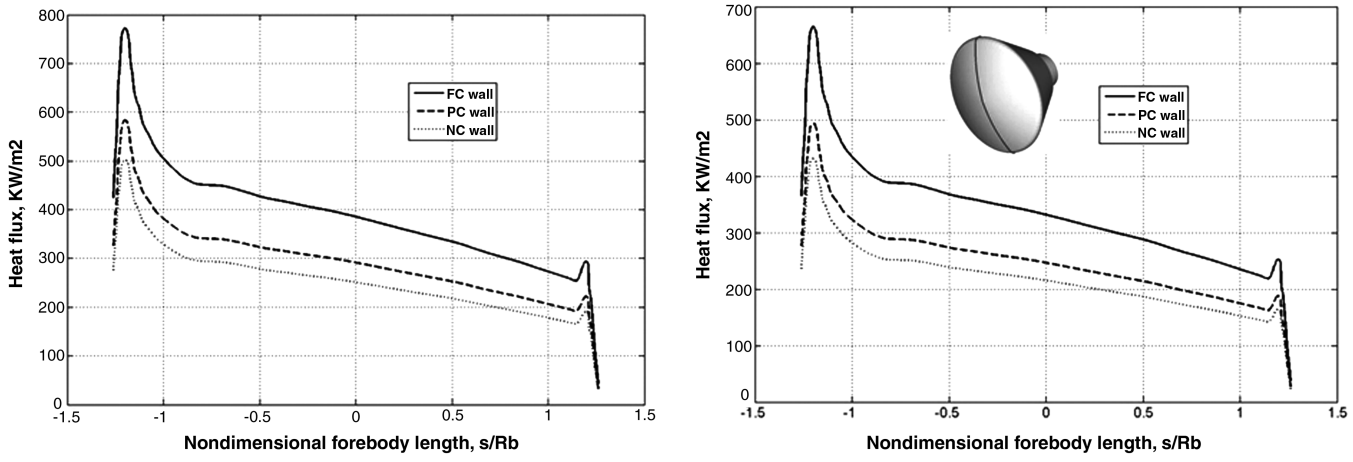

Fig. 24 Heat flux on the forebody capsule centerline for ballistic (left) and lifting (right) trajectory. Vehicle trimmed at $\alpha = 20$ deg with the wall radiative equilibrium condition; comparison among the cases of FC, PC, and NC walls.

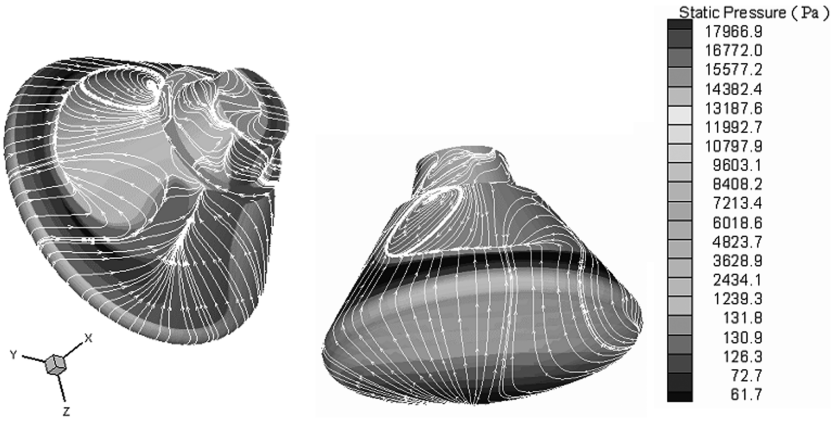

Fig. 25 Pressure distribution and vehicle surface flow patterns at $M_\infty = 19$, AOA $= 20$ deg, $H = 57$ km for reacting-gas computation.

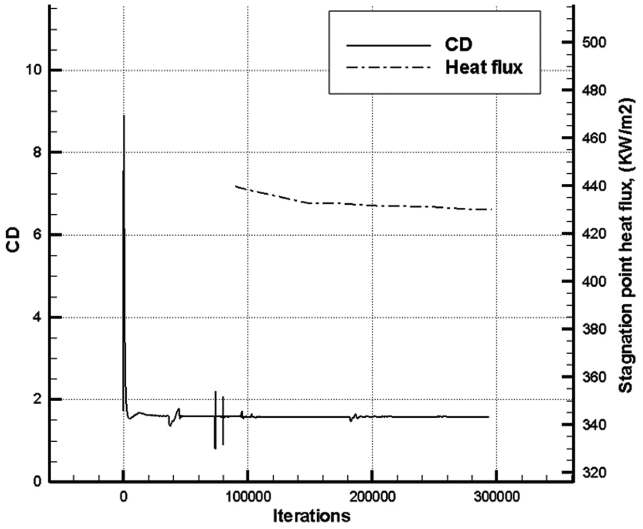

Fig. 26 Convergence history of drag coefficient and stagnation-point heat flux for $M_\infty = 19$, $H = 57$ km and $\alpha = 0$ deg for CFD computation.

interpolating the variable f versus the inverse of the cubic root of the number of cells (representative of a mean value of the cell dimension, $\bar{h}$). For example, Fig. 27 shows the grid sensitivity analysis for both the drag coefficient C_D and the stagnation-point heat flux for the CFD computation at $M_\infty = 19$, $H = 57$ km, and $\alpha = 0$ deg.

The values reported are the L_1, L_2, and L_3 and the Richardson extrapolated values for both L_1-L_2 and L_2-L_3 grid spacing that, in the hypothesis of a spatial second-order scheme and a grid-level ratio equal to 2, can be obtained by means of the following formula:

$$f(\bar{h} = 0) \cong \tfrac{4}{3} \cdot f_{L_{i+1}} - \tfrac{1}{3} \cdot f_{L_i} \tag{10}$$

To account for the uncertainty due to the grid dependence of the variable, both the Richardson extrapolated values and the grid convergence index (see the error bars in Fig. 27) are used.

The grid convergence index (GCI) on the fine grid L_3 is defined as

$$\mathrm{GCI} = \frac{F_s}{(r^p - 1)} \left| \frac{f_{L3} - f_{L2}}{f_{L2}} \right| \tag{11}$$

where F_S is a safety factor (1.25 for three or more grid levels), r is the ratio between the grid spacing of two grid levels ($r = 2$), and p is the (effective) order of the spatial discretization (not equal to that of theoretical consideration) that can be obtained with the following formula:

$$p = \ell_n \left(\frac{f_{L1} - f_{L2}}{f_{L2} - f_{L3}} \right) \cdot \frac{1}{\ell_n(r)} \tag{12}$$

For a better comprehension, the error bars are located at levels three and two of grid spacing. It is interesting to note that the L_2-L_3 error bar is fully contained within the L_1-L_2 error bar. In addition, as a good convergence factor, we can note that the L_1-L_2 extrapolated value is contained within the L_2-L_3 error bar [21]. Finally, note also that the L_1-L_2 Richardson extrapolation is a good estimation of the level 3 CFD computation.

As a conclusion of this grid convergence analysis, it is worth noting that as a general rule for such a complex geometry, the maximum number of cells used was chosen according to an acceptable estimation of the CPU time.

V. Conclusions

An application of the ENTRY tool aimed at supporting the preliminary design of the reentry phase has been provided for an Apollo-like CRV able to transport up to six crew members and cargo to and from the ISS and, perhaps in the future, to carry explorers to the moon and Mars. In this framework, a possible LEO reentry scenario and associated aeroheating environment have been generated and

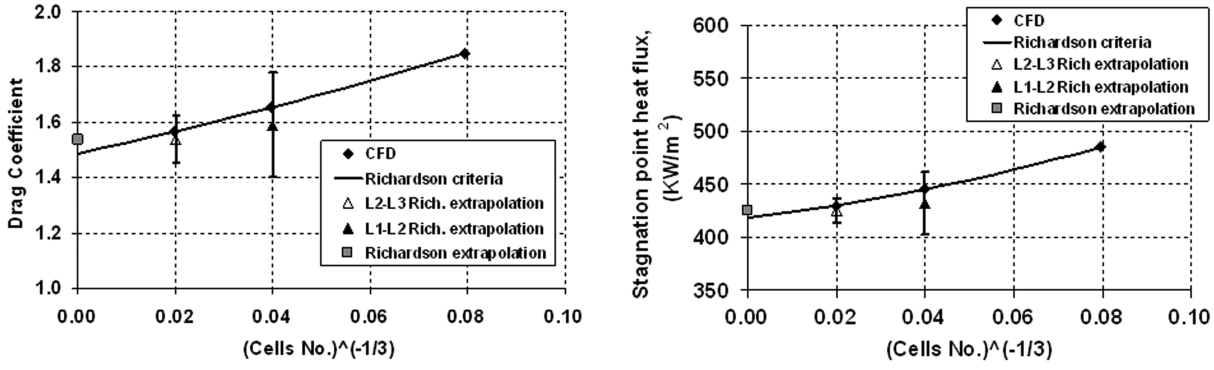

Fig. 27 Grid sensitivity analysis: drag coefficient and stagnation-point heat flux at $M_\infty = 19$, $H = 57$ km and $\alpha = 0$ deg, for L_1, L_2, and L_3 grid levels.

analyzed. Then, using numerical simulations, the flowfield around the vehicle has been investigated at different flight conditions such as those of reentry trajectory peak heating.

Results from numerical simulations, flight data, and wind-tunnel tests have been presented and compared. CFD results agree well with the experimental data and have shown that flow physics can have a great impact on CRV aerodynamics and aerothermodynamics. Results also show that real-gas effects mark the front-shield section pressure distribution by magnifying flow expansion on the leeward part while increasing compression near the stagnation point and shifting this point toward the shoulder. Moreover, the comparison of results shows that present CFD simulations are consistent with flight reconstruction trends: in particular, they show the relevance of some real-gas effects in the high hypersonic range.

Effects of finite rate chemistry on the flowfield around the CRV in a reentry flight have been also highlighted. In particular, at $M_\infty = 16$, no differences are expected for the aerodynamic coefficients when switching from Dunn–Kang kinetics to Park kinetics, whereas at $M_\infty = 19$, a difference of about 2% is observed for the value of C_L and of about 5% for the value of C_{My}.

Finally, present CFD results underline that as far as the capsule aeroheating is concerned, the maximum heat flux at capsule corner, which depends on wall catalycity, is equal to about 800 $\mathrm{kW/m^2}$ and is reached at the peak heating of ballistic reentry trajectory for an FC cold-wall boundary condition.

References

[1] Balakrishnan, A., Davy, W. C., and Lombard, C. K., "Real-Gas Flowfields About Three-Dimensional Configurations," *Journal of Spacecraft and Rockets*, Vol. 22, No. 1, 1985, pp. 46. doi:10.2514/3.25708

[2] Park, C., and Yoont, S., "Calculation of Real-Gas Effects on Blunt-Body Trim Angles," *AIAA Journal*, Vol. 30, No. 4, 1992, pp. 999–1007. doi:10.2514/3.11020

[3] Hassan, B., Candler, G. V., and Olynick, D., "Thermo-Chemical Nonequilibrium Effects on the Aerothermodynamics of Aerobraking Vehicles," *Journal of Spacecraft and Rockets*, Vol. 30, No. 6, 1993, pp. 647–655. doi:10.2514/3.26369

[4] Putnam, Z. R., Braun, R. D., Rohrschneider, R. R., and Dec, J. A., "Entry System Options for Human Return from the Moon and Mars," AIAA Atmospheric Flight Mechanics Conf., AIAA Paper 2005-5915, San Francisco, Aug. 2005.

[5] Tran, Ph., Pault, J. C., and Boukhobza, P., "Re-Entry Flight Experiments Lessons Learned—The Atmospheric Reentry Demonstrator ARD," NATO Rept. RTO-EN-AVT-130, 2007.

[6] Anderson, J. D., *Hypersonic and High Temperature Gas Dynamics*, McGraw–Hill, New York, 1989.

[7] Mitcheltree, R. A., and Gnoffo, P. A., "Thermochemical Nonequilibrium Issues for Earth Re-Entry of Mars Mission Vehicles," *Journal of Spacecraft and Rockets*, Vol. 28, No. 5, 1991, pp. 552–559. doi:10.2514/3.26280

[8] Riabov, V. V., "Simulation Techniques in Hypersonic Aerodynamics," International Astronautical Congress Paper 181, Toronto, 8–13 Sept. 2002.

[9] Wood, W. A., "Hypersonic Pitching-Moment Shift for Stardust Reentry Capsule Forebody," NASA TM-206266, 1997.

[10] Bertin, J. J., *Hypersonic Aerothermodynamics*, AIAA Education Series, AIAA, Washington, D.C., 1994.

[11] Fay, J. A., and Riddell, F. R., "Theory of Stagnation Point Heat Transfer in Dissociated Air," *Journal of the Aeronautical Sciences*, Vol. 2, No. 25, 1958, pp. 73–85.

[12] Anderson, L. A., "Effects of Surface Catalytic Activity on Stagnation Heat Transfer Rates," *AIAA Journal*, Vol. 11, No. 5, 1973, pp. 649–656. doi:10.2514/3.6806

[13] "Capsule Aerothermodynamics," AGARD Rept. 808, Neuilly-sur-Seine, France, 1997.

[14] Ranuzzi, G., and Borreca, "CLAE Project. H3NS: Code Development Verification and Validation," Centro Italiano Ricerche Aerospaziali, Rept. CF-06-1017, Capua, Italy, 2006.

[15] Gupta, R. N., Yos, J. M., Thompson, R. A., and Lee, K. P., "A Review of Reaction Rates and Thermodynamic and Transport Properties for an 11-Species Air Model for Chemical and Thermal Nonequilibrium Calculations to 30,0000 K," NASA RP-1232, 1990.

[16] Park, C., Lee, and Seung-Ho, "Validation of Multi-Temperature Nozzle Flow Code Noznt," 28th AIAA Thermophysics Conf., AIAA Paper 93-2862, Orlando, FL, 6–9 July 1993.

[17] Gnoffo, P. A., Gupta, R. N., and Shinn, J., "Conservation Equations and Physical Models for Hypersonic Air Flows in Thermal and Chemical Nonequilibrium," NASA TP 2867, Feb. 1989.

[18] Walpot, L., "Numerical Analysis of the ARD Capsule in S4 Wind Tunnel," *Proceedings of the 4th European Symposium Aerothermodynamics for Space Applications*, SP-487, ESA, Noordwijk, The Netherlands, March 2002.

[19] Bertin, J. J., "The Effect of Protuberances, Cavities, and Angle of Attack on the Wind-Tunnel Pressures and Heat-Transfer Distribution for the Apollo Command Module," NASA TM X-1243, 1966.

[20] Crowder, R. S., and Moote, J. D., "Apollo Entry Aerodynamics," *Journal of Spacecraft and Rockets*, Vol. 6, No. 3, 1969, pp. 302–307. doi:10.2514/3.29589

[21] Roncioni, P., Rufolo, G. C., Votta, R., and Marini, M., "An Extrapolation-to-Flight Methodology for Wind Tunnel Measurements Applied to the PRORA-USV FTB1 Vehicle," International Astronautical Congress Paper 06-D2.3.09, Valencia, Spain, 2–6 October 2006.

[22] Lees, L., "Laminar Heat Transfer over Blunt-Nosed Bodies at Hypersonic Speeds," *Jet Propulsion* Vol. 26, No. 4, 1956, pp. 259–269.

T. Lin
Associate Editor